EEET ECOLOGICAL ENGINEERING & ENVIRONMENTAL TECHNOLOGY

Ecological Engineering & Environmental Technology, 2026, 27(8), 1–16
https://doi.org/10.12912/27197050/224439
ISSN 2719–7050, License CC-BY 4.0

Received: 2026.05.25
Accepted: 2026.07.10
Published: 2026.08.01

Synthesis of anatase titanium dioxide nanostructures via chitosan-polyvinyl alcohol templating for effective reduction of hexavalent chromium

Ta Thi Huong[1*], Tran Y Doan Trang[1], Vu Dinh Giap[1], Hoang Thanh Duc[1], Pham Huong Quynh[1], Vu Thi Cuong[1]

[1] HaUI Institute of Technology, Hanoi University of Industry, Hanoi 100000, Vietnam
* Corresponding author's e-mail: huongtt@haui.edu.vn

ABSTRACT

Hexavalent chromium (Cr(VI)) is a serious environmental and health problem due to its high toxicity, carcinogenicity, and mobility in aquatic systems. This study presented a new sol-gel synthesis of porous anatase titanium dioxide (TiO_2) nanostructures using chitosan and polyvinyl alcohol (PVA) as templating agents, which enhance surface area and accessibility for Cr(VI) remediation. The organic templates allow for homogenous dispersion of the titanium precursor, resulting in a gel network. Calcination at 400°C provides mesoporous TiO_2 with a BET surface area of 70 m^2/g and predominant pore sizes of 2–5 nm. Raman spectroscopy identified anatase peaks at 145 cm^{-1} and 390–640 cm^{-1}. Post-treatment spectra showed high fluorescence, indicating Cr(III) inclusion after Cr(VI) reduction. FTIR examination revealed increased hydroxyl groups and Cr-O bonds following treatment, with a shift in zeta potential from −57.2 mV to −48.1 mV, indicating Cr(III) surface adsorption and suspension stability. Under visible light, the material effectively reduces Cr(VI) to less harmful Cr(III) or other Cr-containing compounds that remain on the surface of the material. This strategy provides a low-cost, environmentally friendly option for wastewater treatment, balancing high adsorption capacity with photocatalytic effectiveness, and demonstrates the promise of biopolymer-templated nanomaterials for heavy metal remediation.

Keywords: anatase, titanium dioxide, response surface methodology, zeta potential analysis, BET, FITR, XRD, Raman, hexavalent chromium removal.

INTRODUCTION

Chromium (Cr) is commonly identified as a contaminant in aquatic ecosystems, with hexavalent chromium (Cr(VI)) primarily originating from extensive industrial utilization predominantly from the metallurgical sector (>95% of chromium consumption), followed by refractory and foundry industries (3%) and chemical manufacturing (2%) as well as from applications including electroplating, textile dyeing, paints, and wood preservation. Chromium is mostly found in water and wastewater as Cr(III) and Cr(VI) (Hyo et al., 2018; Ghosh et al., 2017). Cr(VI) is the most harmful form because it lasts longer and is much more toxic, causing mutations and cancer, and damaging organs like the lungs, kidneys, and liver, as well as suppressing the immune system. Cr(III) is usually less toxic and can be an important trace element in metabolism (Ghosh et al., 2017; Liang et al., 2013). With rapid industrialization, heavy metal pollution has become a serious environmental issue. Chromium (Cr), released from industries such as electroplating, metallurgy, and textiles, mainly exists in the environment as Cr(III) and Cr(VI) (Liang et al., 2013; Farooqi et al., 2021). While Cr(III) is an essential trace element, Cr(VI) is highly toxic and carcinogenic, with toxicity about 100 times greater and higher solubility and mobility in water and soil (Hu et al., 2020). Consequently, Cr(VI) is classified as a priority hazardous pollutant by the U.S. EPA. Among

remediation approaches, adsorption reduction is considered an effective and cost-efficient method for Cr(VI) removal (Chaudhary et al., 2020).

Among the diverse range of environmental treatment materials, chitosan-based materials are attractive for water purification due to abundant amino and hydroxyl groups, good biocompatibility, biodegradability, low toxicity, hydrophilicity, reactivity, and low cost (Chaudhary et al., 2020; Wang and Zhuang, 2018). These functional groups enable strong binding with heavy metals, making chitosan widely used for wastewater treatment (Lei et al., 2020; Cay et al., 2014). However, pristine chitosan suffers from limited stability and weak thermo-mechanical properties, and porosity (Lei et al., 2020). To address these drawbacks, chitosan membranes are often modified, especially via chemical cross-linking (e.g., glyoxal, glutaraldehyde, epichlorohydrin) to improve structural integrity and mechanical strength, while also enhancing adsorption performance (Kumar et al., 2009; Sahu et al., 2009). In addition, chitosan provides mild antibacterial and antioxidant effects that may further support water purification (Sahu et al., 2009; Xiaoshu et al., 2013; Isawi, 2020). However, pure chitosan has several drawbacks, such as low thermomechanical strength, high swelling, and poor water stability (Xiaoshu et al., 2013). Therefore, combining chitosan with poly (vinyl alcohol) (PVA) enhances the formation of a hydrogen-bonded polymer network, improves mechanical integrity, stabilizes the membrane/hydrogel/particle morphology, and modifies swelling and porosity to enhance mass transfer and improve pollutant accessibility to active sites of chitosan (Xiaoshu et al., 2013; Isawi, 2020; Attia et al., 2020). As a result, the composite material between these two combinations is considered a green, easy-to-process adsorption platform that can be further enhanced by cross-linking or by incorporating inorganic fillers to improve removal efficiency and reusability in water pollution treatment (Isawi, 2020).

With its excellent thermal stability and low toxicity, titanium dioxide (TiO_2) is a widely used pigment and photocatalyst with great promise for water and environmental remediation (Neghi et al., 2019; Wang et al., 2018; Anaya-Esparza et al., 2019). TiO_2 can enhance mechanical/physicochemical properties, UV shielding, and antibacterial activity against S. aureus and E. coli when incorporated into chitosan membranes [18-20]. On the other hand, high TiO_2 loading may lead to nanoparticle aggregation, thereby impairing membrane dynamics and reducing the number of chitosan binding sites available for metal ions (Huang et al., 2014; Xu et al., 2021; Du et al., 2020). The reported chitosan/TiO_2 composites remove heavy metals through adsorption, although many studies report capacities below 100 mg/g, which are frequently associated with high TiO_2-to-chitosan ratios (Duan et al., 2020). This suggests that lower TiO_2 content may better balance adsorption performance with just a slight loss of photocatalytic effectiveness (Li et al., 2021).

To extend the activity into the visible-light range, it is usually necessary to create mid-gap states via doping or defect engineering (Zainal et al., 2009; Wiacek et al., 2018; Vallejo-Montesinos et al., 2020). The majority of TiO_2 photocatalysis research relies on UV or simulated sunlight. In addition to photocatalysis, TiO_2 can generate reactive oxygen species (ROS), which facilitate antimicrobial activity. When combined with the intrinsic (weak) antibacterial activity of chitosan, synergistic bactericidal performance can be achieved (Jurado-Manzano et al., 2019; Bahloul et al., 2020; Karabassi et al., 2020).

In addition, researchers tend to apply mathematical models, such as response surface methodology (RSM) to reduce the large number of experiments required, while enabling a systematic examination of how process factors and desired output responses are affected by input conditions—such as pH, the initial concentration of Cr(VI) in the solution, and the dosage of the adsorbent/material used for pollutant removal. These are among the most basic variables regularly used for assessment, providing useful information for determining optimal operating settings and clarifying the underlying removal mechanism.

Due to the advantageous properties of chitosan, polyvinyl alcohol combined with titanium oxide forms a promising material for addressing environmental problems. However, instead of utilizing the inherent functional groups in each material, the research team sought to improve the material to create a new one where chitosan and PVA are used as soft molds and network-forming agents to evenly disperse the titanium precursor, shape the gel structure, and create porosity after calcination; when calcined in air, the organic phase is removed, leaving a porous TiO_2 framework with high surface area and mass transfer capacity, thereby improving the efficiency of metal ion removal through surface hydroxyl groups (Ti–OH).

MATERIALS AND METHODS

Material

In this study, chitosan was used in flake form (moisture content: < 10%; pH: 7.0->8.0) supplied by S-Green Investment Joint Stock Company. Polyvinyl alcohol with the following characteristics: melting point: 200 °C; density: 1.19 g/cm, was supplied by Mephalab Equipment and Materials CO., LTD. Titanium(IV) isopropoxide (assay 97%; liquid form) from Sigma Aldrich, was supplied by Glam Group CO., LTD. Potassium dichromate $K_2Cr_2O_7$ (orange-red monoclinic crystals; soluble in water; insoluble in ethanol, with strong oxidizing properties), was provided by Dongzheng Chemical group. In addition, 2.83 gram Potassium dichromate was dissolved in 1 Lit of distilled water, the solution is the stock for subsequent dilutions. Besides, 1.5 Diphenylcarbazide 98% (Duksan, Bottle 25G, Cas 140-22-7) has assay > 98%; provided by Duksan Korea Company, was used to evaluate hexavalent chromium residual concentrations by using Ultraviolet-visible light spectrophotometer (Uv Visible Spectrophotometer, 320–1100 nm).

The process of material fabrication by the sol-gel method consists of the following stages

Step 1: Solution 1 was prepared by dissolving 2 gram of chitosan flake in 5 ml acetate solution. The mixture was homogenized entirely and 8 grams of (PVA) were added under continuous stirring with a magnetic stirrer at 200 rpm.

Step 2: Solution 2 was prepared by adding 20 mL titanium (IV) isopropoxide to 30 mL isopropanol.

Step 3: Solution 2 was added dropwise to the mixture obtained in Step 1 under magnetic stirring, while maintaining a temperature of approximately 4°C by placing an ice bath around the flask for 3 hours. After the addition is complete, continue stirring the mixture for 1 more hour.

Step 4: The resulting mixture was dried at 80 °C for 24 hours.

Step 5: The dried solid obtained in Step 4 was calcined at 400 °C for 5 hours. The final solid was then stored for characterization and for evaluating its ability to remove heavy metals (hexavalent chromium).

Experimental and model development

In this study, a central composite design (CCD) based on response surface methodology (RSM) was employed to investigate the individual, interactive, and antagonistic effects of three main factors (variables), namely: pH (denoted as A), initial Cr(VI) concentration (mg/L, denoted as B), and adsorbent dosage (g/L, denoted as C) (Li et al., 2021; Zainal et al., 2009; Wiacek et al., 2018). Their levels are presented in Table 1, where the center points, factorial points, and axial (star) points are coded as 0, ±1, and ±α, respectively; here, α represents the distance from the center point to the axial points. The value of α is given by $(2k)^{1/4}$, where k is the number of experimental factors (Karbassi et al., 2020). The complete experimental design matrix (Table 2) shows the required factor combinations according to CCRD to develop an empirical model for evaluating the effect of each factor on Cr(VI) adsorption. In total, 20 experimental runs were conducted, including 8 factorial runs, 6 axial runs, and 6 center point runs (Sahu et al., 2009).

Material characteristics

The properties of titanium dioxide material are demonstrated through several basic analyses such as X-ray diffraction (XRD - XRD Model: EMMA); scanning electron microscopy (SEM - SEM; JEOL, Japan); energy-dispersive X-ray spectroscopy; and Fourier transform infrared spectroscopy (FTIR - Nicolet iS5, Thermo Fisher Scientific, US), these machine help determine the morphology, crystal structure, and elemental composition of the sample, as well as identify the functional groups formed on the titanium dioxide sample synthesized through this research. Furthermore, zeta potential analysis was also used

Table 1. Experimental factors for the removal of Cr(VI) from water by material anatase TiO_2

	Factors	Units	Levels				
			-α	-1	0	1	+α
A	pH		1.5	4	6.5	9	11.5
B	Cr(VI) concentration	mg/L	0	25	50	75	100
C	Adsorbent	g/L	0	1	2	3	4

Table 2. Experimental design matrix and response of experimental settings for Cr(VI) removal by Anatase TiO_2 adsorbent

Run	Factors		
	A	B	C
	pH	Cr(VI) concentration	Adsrobent
1	6.5	50	2
2	6.5	50	2
3	2.29	50	2
4	6.5	50	2
5	4	75	1
6	4	25	1
7	6.5	50	2
8	6.5	7.9	2
9	6.5	50	3.7
10	9	75	1
11	6.5	50	0.3
12	4	25	3
13	6.5	92.04	2
14	6.5	50	2
15	9	25	3
16	9	75	3
17	4	75	3
18	10.7	50	2
19	6.5	50	2
20	9	25	1

for evaluating the stability and surface properties of liquid dispersion systems of the material. Raman spectroscopy was used to determine the chemical composition, molecular structure, phase of materials, crystallinity, and stress/strain of solids. Besides, Brunauer-Emmett-Teller analysis was conducted to determine the specific surface area of the material in this research.

RESULT AND DISCUSSION

Model creation, verification, and diagnosis analysis

For the CCD-RSM experiment, the study was conducted under the reaction conditions shown in Table 2 at room temperature, with each experiment lasting 3 hours. The residual Cr(VI) values after each experiment were then determined using the same method with a UV-vis instrument. Table 3 below provides information on the experimental and predicted results for each experiment. The Cr(VI) processing efficiency based on the CCD experimental conditions is listed in Table 2. In addition, experimental and simulation results are also shown in Table 3. Based on the experimental results and the predictive model, the relationship between the output factor, Cr(VI) processing efficiency, and the input factors is shown as follows:

$$\text{Cr(VI) } removal\ (\%) = 10.2 - 19.4A - \\ - 1.76B + 6.51C + 4.6AB - 8.4AC + 4BC + \\ + 12.16\,A^2 + 8.54B^2 - 0.1405C^2 \quad (1)$$

The quadratic coefficients in Equation 1 represent the linear terms. Negative signs indicate antagonistic effects, while positive signs indicate synergy from a single factor or a combination of both factors. The model's predicted $R^2 = 0.8172$ and adjusted $R^2 = 0.9546$ (difference < 0.2) and $R^2 = 0.9761$ indicate suitable predictive performance. Adeq precision = 20.99 confirms the model's reasonable signal-to-noise ratio, indicating sufficient signal to explore the design space (Table 4).

The quadratic model is highly significant for characterizing Cr(VI) removal effectiveness, as indicated by the ANOVA results ($F = 45.36$, $p < 0.0001$). This means that there is very little chance of achieving such a huge F-value due to random noise. With $R^2 = 0.9761$ and Adjusted $R^2 = 0.9546$, the model also has a strong goodness-of-fit, indicating that it accounts for most of the response variability. The linear terms show that pH (A) is the most relevant factor ($F = 183.36$, $p < 0.0001$), followed by the initial Cr(VI) concentration (B) ($F = 67.42$, $p < 0.0001$) and the adsorbent dosage/Anatase TiO_2 mass (C) ($F = 20.62$, $p = 0.0011$). This suggests that pH significantly influences Cr(VI) removal, as do the initial concentration and the adsorbent dose.

The linear terms show that pH (A) is the most relevant factor ($F = 183.36$, $p < 0.0001$), followed by the initial Cr(VI) concentration (B) ($F = 67.42$, $p < 0.0001$) and the adsorbent dosage/Anatase TiO_2 mass (C) ($F = 20.62$, $p = 0.0011$). This implies that the initial concentration, the adsorbent dosage, and pH all have a major impact on the removal of Cr(VI). This suggests that starting concentration, adsorbent dose, and pH all have a major impact on Cr(VI) removal. In terms of interaction effects, initial Cr(VI) concentration and adsorbent dosage affected p/h and Cr(VI) removal efficiency, and AB ($p = 0.0338$) and AC

Table 3. Experimental and predicted Cr(VI) removal by anatase TiO_2 adsorbent

Run	Factors			Response Cr(VI) rmeoval (%)	
	A	B	C	Experimental	Predicted
	pH	Cr(VI) concentration	Adsrobent		
1	6.5	50	2	10.12	10.2
2	6.5	50	2	9.6	10.2
3	2.29	50	2	85.3	77.23
4	6.5	50	2	9.8	10.2
5	4	75	1	10.4	14.89
6	4	25	1	50.2	55.62
7	6.5	50	2	10	10.2
8	6.5	7.9	2	62	54.14
9	6.5	50	3.7	23	20.74
10	9	75	1	4.1	2.09
11	6.5	50	0.3	3.7	1.14
12	4	25	3	70.4	77.34
13	6.5	92.04	2	13.8	14.57
14	6.5	50	2	9.95	10.21
15	9	25	3	12.1	12.63
16	9	75	3	6.7	6.3
17	4	75	3	52	52.07
18	10.7	50	2	11.01	11.97
19	6.5	50	2	10.5	10.22
20	9	25	1	20.1	24.42

Table 4. Analysis of variance (ANOVA) for a quadratic model representing Cr(VI) removal by anatase TiO_2 adsorbent

Source	Sum of squares	df	Mean square	F-value	p-value	
Model	11444.12	9	1271.57	45.36	< 0.0001	significant
A-pH	5140.45	1	5140.45	183.36	< 0.0001	
B-Cr(VI) concentration	1890.07	1	1890.07	67.42	< 0.0001	
C-ANATASE TIO2 mass	578.16	1	578.16	20.62	0.0011	
AB	169.28	1	169.28	6.04	0.0338	
AC	564.48	1	564.48	20.13	0.0012	
BC	128.00	1	128.00	4.57	0.0584	
A^2	2132.04	1	2132.04	76.05	< 0.0001	
B^2	1050.85	1	1050.85	37.48	0.0001	
C^2	0.2846	1	0.2846	0.0101	0.9217	
Residual	280.35	10	28.04			
Lack of Fit	279.89	5	55.98	599.65	< 0.0001	significant
Pure Error	0.4668	5	0.0934			
Cor Total	11724.47	19				
R^2	0.9761		Predicted R^2	0.8172		
Adjusted R^2	0.9546		Adeq precision	20.9865		

(p = 0.0012) were statistically significant. Furthermore, the curvature of the response surface is shown through A^2 and B^2, with statistically significant p-values < 0.0001. In addition, the empirical values and the predicted values from the model show a good fit, with both values tending to closely follow the diagonal (Figure 1). Three 3D response surface plots from Design-Expert

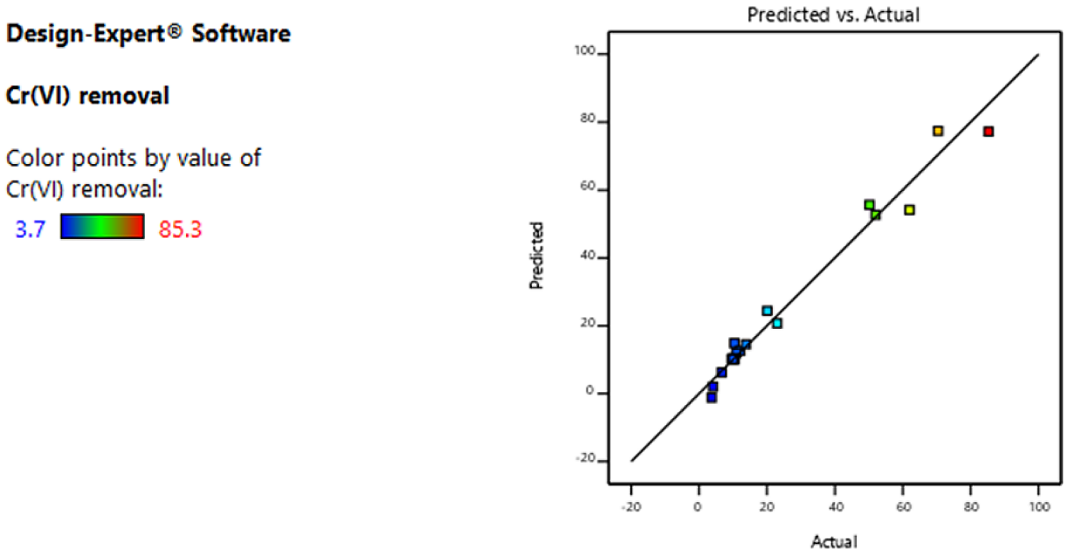

Figure 1. Experimental and predicted results for Cr(VI) removal by anatase TiO_2 adsorbent

are displayed in Figure 2, showing how each factor pair affects the Cr(VI) removal effectiveness (%) while keeping the other factor constant (Factor Coding: Actual). The pH and initial Cr concentration fluctuations are displayed in Figure 2a while maintaining a constant adsorbent mass (C) of 2 g/L. The blue-green region (higher values) is concentrated at low pH and low beginning Cr (VI) concentrations; the surface and contour lines demonstrate a considerable decrease in efficiency as pH increases (less acidic environment) and an increase as the initial Cr (VI) concentration increases. As the initial Cr(VI) concentration is fixed at B = 50 mg/L, Figure 2b illustrates the change in pH and material mass Anatase TiO_2.

Efficiency increases along with material mass and continues to decrease with increasing pH, indicating that high adsorption doses and low pH are more favorable conditions for removal. Figure 6c shows the relationship between the initial Cr(VI) concentration and the mass of the Anatase TiO_2 material while the pH value is fixed at A = 6.5. The trend remains consistent: higher Cr(VI) concentrations lead to lower removal percentage, while increasing the mass of Anatase TiO_2 improves removal percentage. The curved surface shape and elliptical contour lines suggest interaction/non-linearity between factors in the investigated domain. To visually verify model deviations for each experimental condition, experimental points are marked on the surface with red dots indicating actual values greater than anticipated and empty dots indicating actual values lower than predicted.

Adsorption and kinetic studies

Adsorption study

stablished isotherm models were applied to experimental data to determine the adsorption of Cr(VI) by anatase TiO_2 adsorbent. Mathematical expressions describing Langmuir, Freundlich. The Langmuir expression (Kumar et al., 2009; Isawi, 2020) is as follows:

$$\frac{C_e}{Q_e} = \frac{1}{Q_{max}b} + \frac{C_e}{Q_{max}} \tag{2}$$

where: C_e (mg/L) is the equilibrium concentration of the adsorbate, Q_{max} (mg/g) and b (L/mg) are Langmuir characteristic constants that indicate the maximum adsorption capacity and the energy of adsorption, respectively, and Q_e (mg/g) is the quantity of adsorbate adsorbed per mass of adsorbent (Lei et al., 2020; Farooqi et al., 2021).

Adsorption on a heterogeneous surface is assumed by the Freundlich model, which is represented by the equation:

$$LogQ_e = \frac{1}{n} logC_e + logk_f \tag{3}$$

where: C_e (mg/L) is the adsorbate equilibrium concentration, Q_e (mg/g) is the quantity of adsorbate adsorbed per mass of adsorbent, and k_f (mg/g) and $1/n$ are Freundlich characteristic constants that indicate adsorption capacity and adsorption intensity, respectively (Attia et al., 2020; Du et al., 2020).

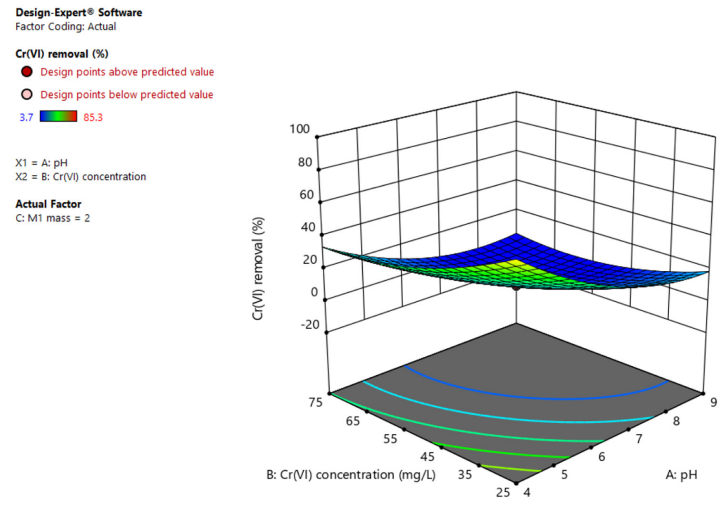

a)

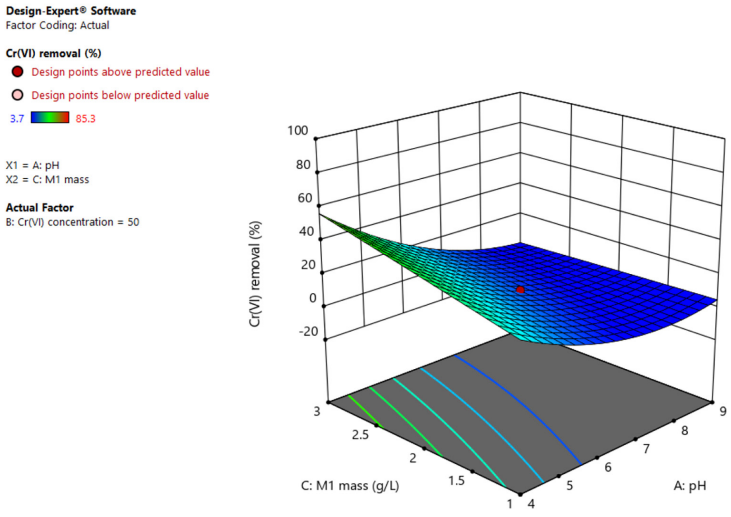

b)

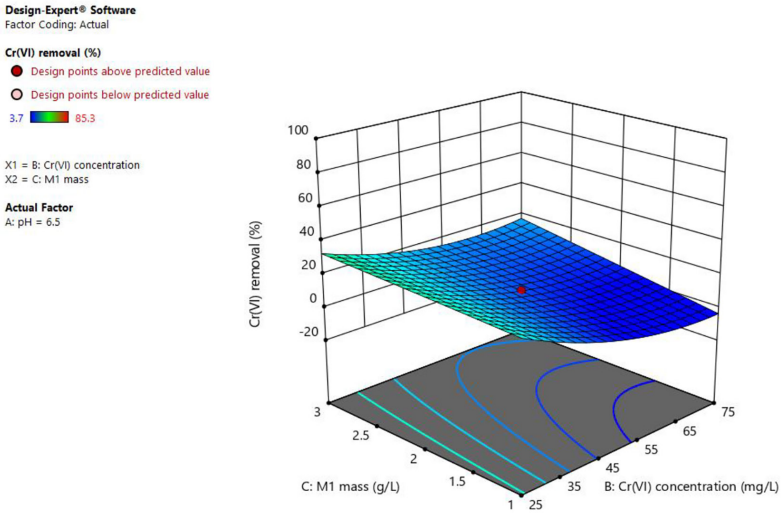

c)

Figure 2. Integrated effects of driving factors on Cr(VI) removal from water by anatase TiO_2 adsorbent. a) pH and Cr(VI) concentration (mg/L) at Anatase TiO_2 dosage = 2 g/L; b) pH and anatase TiO_2 dosage at Cr(VI) concentration = 50 mg/L; c) Cr(VI) concentration (mg/L) and Anatase TiO_2 dosage (g/L) at pH = 6.5

Figure 3 and Table 5 show that the Langmuir model is a better fit than the Freundlich model. Specifically, the linear Langmuir equation (C_e/q_e = 0.006115 C_e + 0.0087) achieves a correlation coefficient R^2 = 0.995, demonstrating that the experimental data fit very well with the hypothesis of monolayer adsorption on a homogeneous surface with adsorption sites having equivalent energies. The maximum adsorption capacity according to the Langmuir model reaches Q_{max} = 163.93 mg/g (approximately 164 mg/g), combined with the Langmuir constant b = 0.701 L/mg, a high value indicating strong adsorption affinity between Cr(VI) and the material surface. Conversely, the Freundlich model (Log q_e = 0.1772 Log C_e + 1.9083) only achieved R^2 = 0.9325, significantly lower than Langmuir. Although the Freundlich parameters still showed favorable adsorption (n = 5.64 > 1) and k_f = 80.97 reflected good adsorption at low concentrations, the overall fit was poorer, suggesting that multilayer adsorption or a heterogeneous surface is not an accurate description of this system.

Kinetic study

Two popular models (called reaction models) used to model time-dependent experimental data of adsorption are the pseudo-first-order (PFO) and the pseudo-second-order (PSO) models (Duan et al., 2020; Li et al., 2021). The equations representing the pseudo-first-order and pseudo-second-order models are shown below (Huong et al., 2025).

$$Pseudo\text{-}first\ order: log\ (q_e - q_t) = = logq_e - \frac{K_1 t}{2.303} \quad (4)$$

$$Pseudo\text{-}second\ order: \frac{t}{q_t} = \frac{1}{K_2 q_e^2} + \frac{t}{q_e} \quad (5)$$

where: K_1 (h^{-1}) and K_2 ($g.mg^{-1}\ h^{-1}$) are the rate constants for the pseudo-first and second order; q_t and q_e are the amount of adsorption capacity at time t and equilibrium time (mg/g), respectively.

The pseudo-second-order model was more appropriate than the pseudo-first-order kinetic model (Figure 4 and Table 6). In particular, the correlation coefficient R^2 = 0.9124 was obtained by the linear equation of PSO (t/qt = 0.0196 t + 0.0573), indicating a satisfactory match across the whole experimental period (0–25 hours). The adsorption rate is directly proportional to the square of the number of remaining vacant sites on the material surface, indicating that chemisorption was the primary rate control step. According to the PSO model, the equilibrium adsorption capacity reached Q_e (51.02 mg/g), rate constant K_2 0.00753 $g.mg^{-1}\ h^{-1}$, suggesting a relatively quick process in the first stage and consistent with ion exchange or complex formation with surface

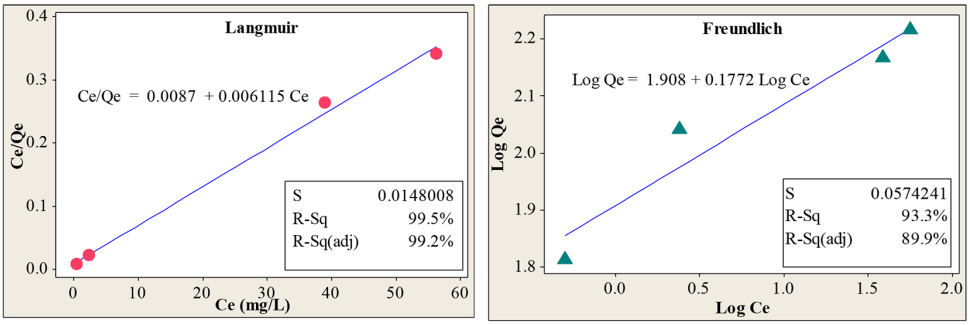

a) b)

Figure 3. Langmuir and Freudlich for Cr(VI) removal by Anatase TiO_2 adsorbent under conditions: pH = 6; adsorbent dosage: 1 g/L; initial Cr(VI) concentrations 25, 50, 100, 150 mg/L, contact time: 5 hours, room temperature: 24 °C

Table 5. Langmuir and Freundlich parameters

Model	R^2	Q_{max} (mg/g)	b (L/mg)	k_f (mg/g)	n
Langmuir	0.9944	163.93	0.701	-	-
Freundlich	0.9325	-	-	80.97	5.64

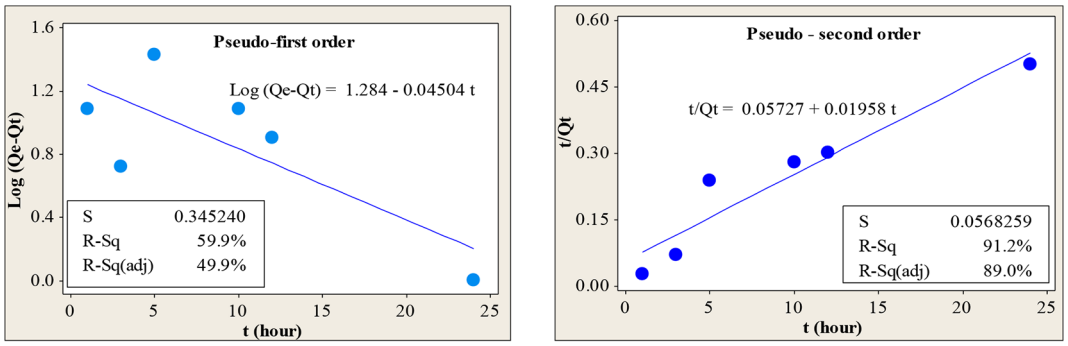

a) b)

Figure 4. Pseudo-first order and Pseudo-second order

functional. On the other hand, the PFO model only obtained R^2 = 0.5989, which is extremely low and clearly inconsistent, particularly at later time periods. The process is not adequately represented by the rate constant K_1 is 0.1036 h^{-1}, and the Q_e value from PFO is only about 19.25 mg/g (lower than Q_e from PSO and Q_{max} from Langmuir is 164 mg/g). The adsorption mechanism is largely chemisorption rather than exclusively physisorption or diffusion-controlled, as confirmed by the poor fit of PFO. This result is completely consistent with the previously established Langmuir isotherm model (R^2 = 0.9944).

Table 6. Pseudo-first and second models' parameters

Pseudo-first order (PFO)	Pseudo-second order (PSO)
K_1 = 0.1036 h^{-1}	K_2 = 0.00753 $g.mg^{-1}$ $^{h-}$1
Q_e = 19.25 mg/g	Q_e = 51.02 mg/g
R^2 = 0.5989	R^2 = 0.9124

Characteristics of the material before and after the removal of hexavalent chromium

X-ray diffraction (XRD) analysis

Figure 5 depicts the X-ray diffraction (XRD) pattern of the Anatase TiO_2 sample, exhibiting a prominent diffraction peak at 2θ approximate 25° along with several distinctive peaks emerging at roughly 2θ = 37–38°, 48°, 54–55°, 62–63° and some weak peaks in the high-angle region (69–70° and 75°) (Duan et al., 2020; Huang et al., 2014; Neghi et al., 2019). This set of peak positions is similar to the properties of titanium oxide (TiO_2) in the anatase phase, where the peak about 25.3° is generally assigned to plane (101) and acts as the phase identification peak (Wang et al., 2018; Wiacek et al., 2018; Bahloul et al., 2020). In addition, the spectrum does not show the typical strong peak of the rutile phase at about 2θ =

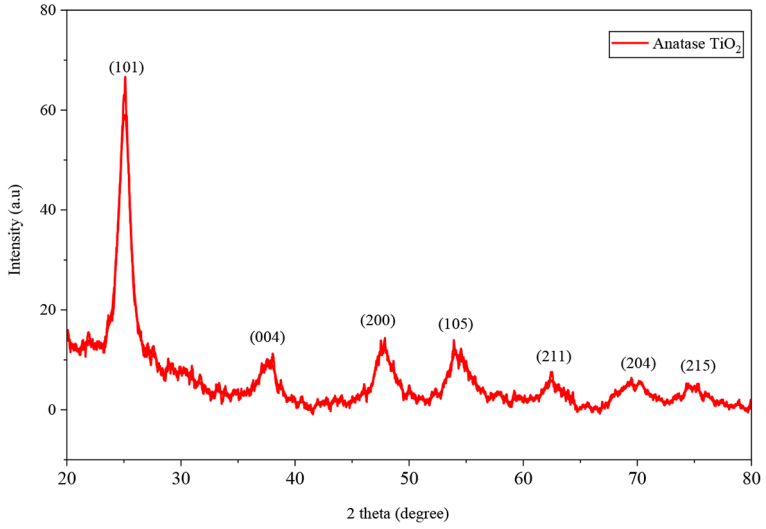

Figure 5. XRD analysis for anatase TiO_2 adsorbent

27.4° (plane (110)), indicating that the sample mostly resides in the anatase form (Ahmad et al., 2021; Vallejo-Montesinos et al., 2020).

Fourier transform infrared spectroscopy (FTIR) analysis

The FTIR spectra of the material following Cr(VI) treatment and as-synthesized TiO_2 are shown in Figure 6. Surface –OH groups are primarily responsible for a wide band at 3200–3600 cm^{-1}. The TiO_2 structure is confirmed by distinct Ti–O and Ti–O–Ti peaks (Huang et al., 2014; Neghi et al., 2019). Polymer signals (C–H from 2850–2920 cm^{-1}, amide/amine, strong C–O–C at 1000–1200 cm^{-1}) are severely diminished or absent (residual traces presumably from incomplete combustion) since chitosan/PVA served only as a template/binder and was mostly eliminated by oxidative calcination. Notable alterations following Cr(VI) treatment include stronger adsorption and a higher surface hydroxyl density, resulting from increased intensity and width of the –OH and H–O–H bands. Besides, modifications/shifts in the 800–1000 cm^{-1} and Ti–O/Ti–O–Ti areas indicate that complexation between surface –OH groups and Cr(VI) (chromate/dichromate) (Ahmad et al 2021; Vallejo-Montesinos et al., 2020). These findings validate the successful immobilization of Cr(VI) on the TiO_2 surface when combined with SEM-EDX evidence of Cr presence

Scanning electron microscopy (SEM); energy-dispersive X-ray spectroscopy (EDX) analysis

The SEM images of the anatase TiO_2 sample (Figure 7a, 2 µm scale bar) reveal a relatively dense and fairly smooth surface composed of

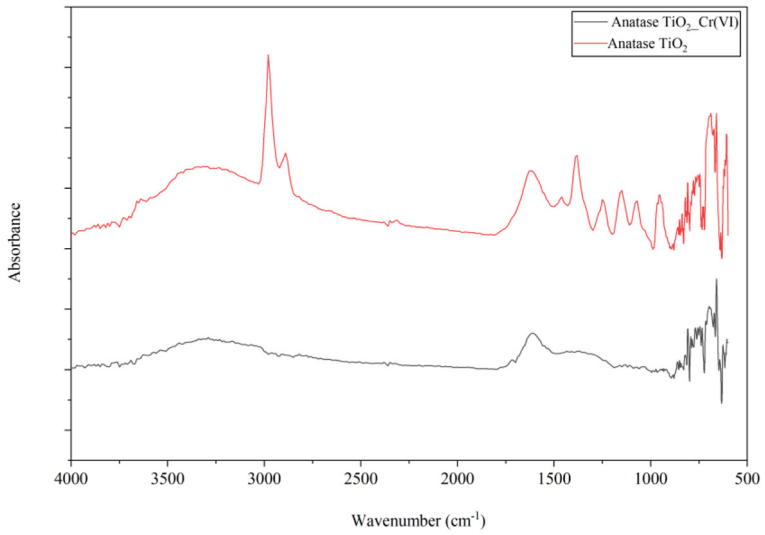

Figure 6. FITR analysis anatase TiO_2 (before removal Cr(VI)) and Anatase TiO_2-Cr(VI) (orginal adsorbent after removing Cr(VI))

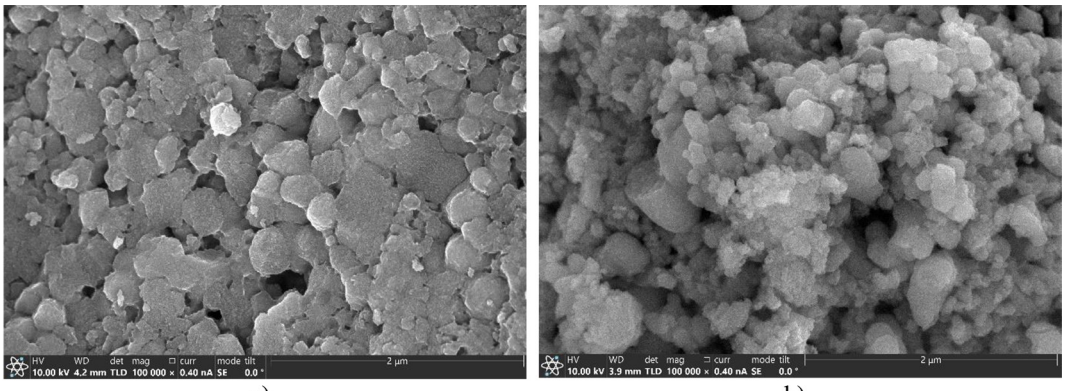

Figure 7. (a) SEM image of anatase TiO_2 before treatment; (b) SEM image of anatase TiO_2 after Cr(VI) treatment

compact agglomerated domains, where particles are tightly fused into a continuous structure with only a limited number of interparticle voids and a low coverage of fine particulates. After Cr(VI) treatment (Figure 7b), the surface morphology changes markedly, becoming rougher and more heterogeneous; larger agglomerates form, extensively decorated with fine/submicron particles coating the surface and surrounding the clusters, which partially mask or fill the interparticle pores. The increased surface roughness and the appearance of a deposited fine layer after treatment suggest the adsorption and/or deposition of Cr-containing species on the material surface.

EDX result

To support the assessment of the capability of the material for Cr(VI) removal, EDX analysis was performed to verify the presence of chromium on the sample surface after the adsorption process. The EDX results show that, in addition to the dominant elements of the material matrix (Ti and O), the post-treatment sample exhibits a detectable Cr signal (at a trace level), providing direct evidence that Cr-containing species were retained on the surface of Anatase TiO_2 after adsorption.

The EDX spectrum of anatase TiO_2 is shown in Figure 8a, with estimated concentrations of Ti = 43.5 wt% and O = 45.0 wt%, as well as C = 10.6 wt%, which may be from residual organic matter from the high-temperature ashing of chitosan and PVA, and a trace quantity of Na: 0.9 wt%. The Anatase TiO_2 –Cr(VI) sample exhibits a detectable Cr signal of about 0.3 weight percent (±0.1) after being treated with Cr(VI), but it still has strong Ti and Oxygen signals. Interestingly, Ti dropped sharply from 43.5 to 28.8 weight percent while oxygen increased somewhat from 45 to 59.7 weight percent, indicating that an oxygen-rich layer developed on the surface after adsorption. This is consistent with the sample's coarser morphology observed in the SEM images after Cr(VI) treatment. This examination indicates that the substance has removed Cr(VI).

Zeta potential analysis

Figure 9 displays the zeta potential analysis results, which show that the initial anatase TiO_2 material exhibited a negative surface charge of -57.2 mV. This suggests that the stability of the suspension system is caused by electrostatic repulsion between the particles. For the Cr(VI)-treated material, the surface charge reduced marginally to -48.1mV, 9mV changing from the material's initial surface charge. This demonstrates that Cr(VI) was transformed, resulting in Cr^{3+} or other Cr-containing compounds with a lower negative charge than the original material. As a

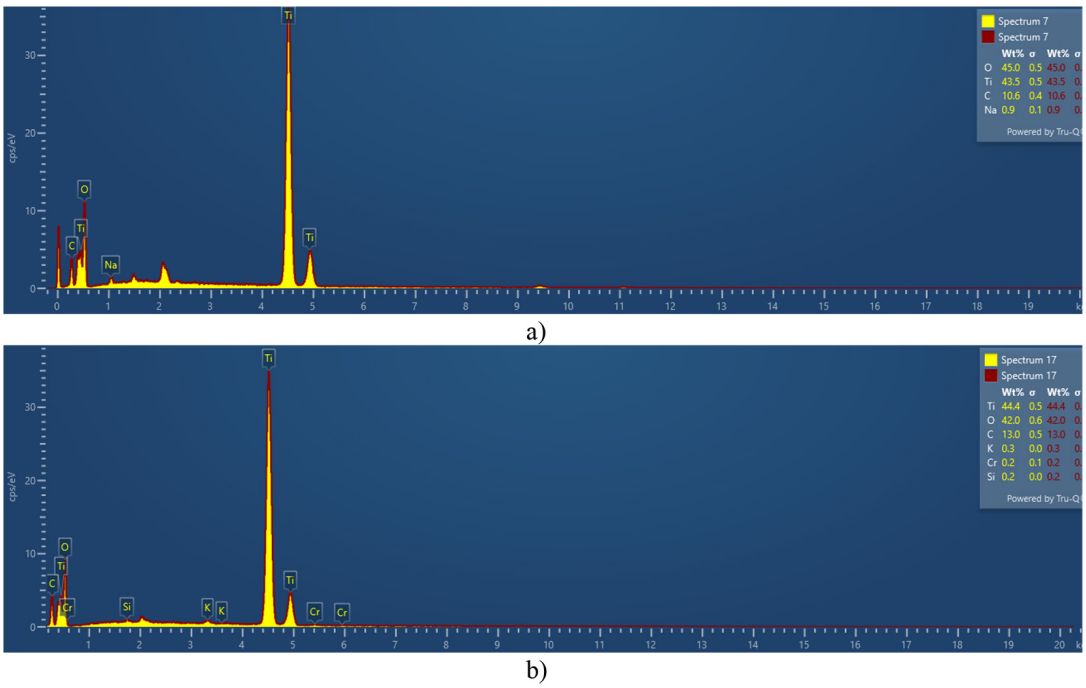

Figure 8. a) EDX spectrum of anatase TiO_2 showing dominant Ti and O signals; b) EDX spectrum of Anatase TiO_2 –Cr revealing an additional Cr signal (anatase TiO_2 – Cr(VI))

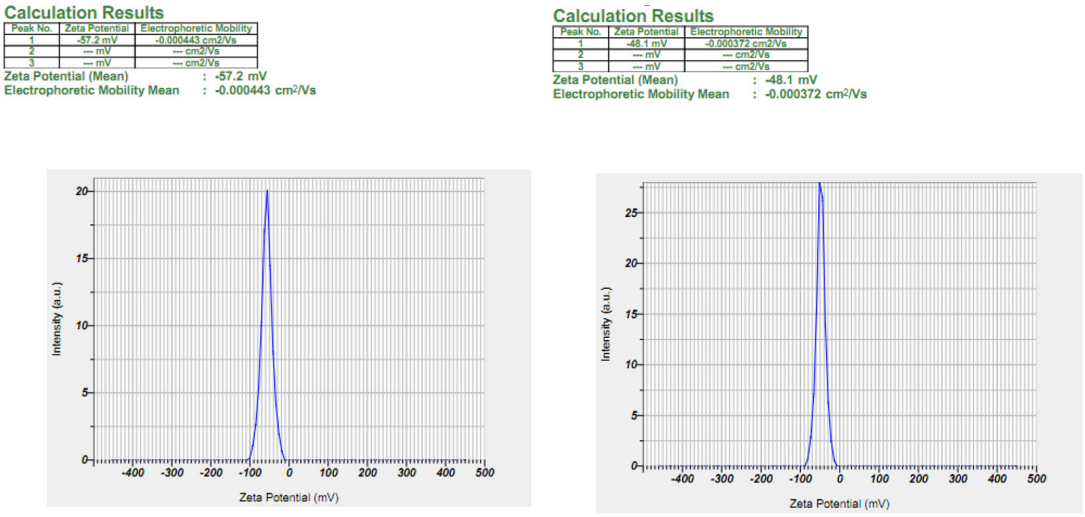

a) Anatase TiO_2 b) Anatase TiO_2 – Cr(VI)

Figure 9. Zeta potential analysis for anatase TiO_2 and anatase TiO_2 – Cr(VI)

result, when they attached to and infiltrated the TiO_2 crystal lattice, they altered the surface of the material, but only a small amount of it was covered. However, the shift was not large, thus the suspension remained stable and easy to disperse. This finding demonstrates that the material can handle Cr(VI) and that the pollutant is maintained on its surface.

Raman spectroscopy

This study employs Raman spectroscopy analysis to precisely re-determine the TiO_2 structure, crystallinity, and surface of the material before and after Cr(VI) treatment. This enables accurate determination of both the material structure and the Cr(VI) treatment method.

Figure 10 displays the typical E_g peak of TiO_2's anatase phase, which is at 145 cm^{-1}. In addition, many minor peaks emerge in the 390–640 cm^{-1} range, indicating the presence of more B_{1g} and A_{1g} anatases. These peaks appear in both the material before and after Cr(VI) treatment, and no new peaks arise; only a significant change in the measured signal strength of the material is noticed following Cr(VI) treatment. This is a clear sign of intense fluorescence, possibly caused by Cr(VI) being reduced to Cr(III) and penetrating the TiO_2 crystal lattice, resulting in strong photoluminescence. This demonstrates that the material was used to cure Cr(VI).

Brunauer-Emmett-Teller (BET) method

BET method of a physicochemical materials analysis before and after the removal of hexavalent chromium is presented in Figure 11 and Table 7. The BET results for the pristine anatase TiO_2 sample and the sample after Cr(VI) treatment (anatase TiO_2 – Cr(VI)) reveal only minor changes in the porous structure of the material, which are consistent with the photocatalytic reduction

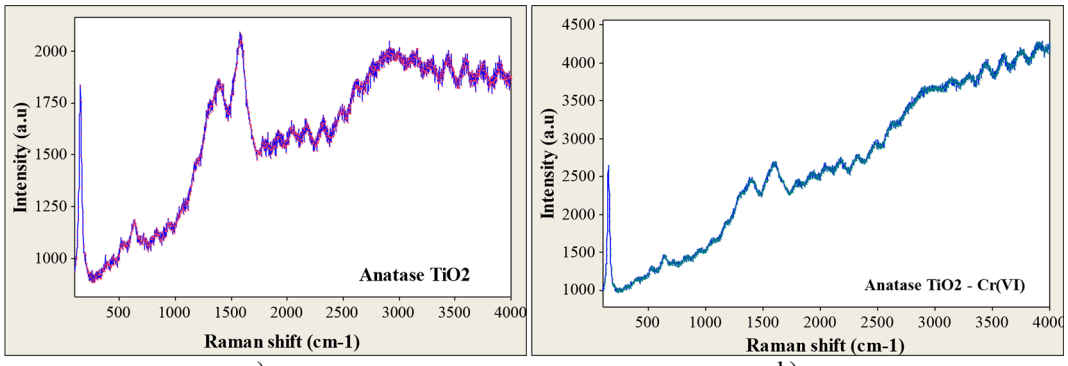

a) b)

Figure 10. Raman spectrum: (a) anatase TiO_2 and (b) anatase TiO_2 – Cr(VI)

mechanism of Cr(VI) to Cr(III), accompanied by the retention of Cr(III) on the surface and within the pores. The total pore surface areas of the pristine anatase TiO_2 are 62.713 m^2/g (BJH adsorption) and 54.4879 m^2/g (BJH desorption), with a BET specific surface area of 70 m^2/g. Depending on the calculation method (BJH or D-H), the average pore width varies between 4.7949 nm and 5.5970 nm, whereas the cumulative pore volume averages roughly 0.075 cm^3/g. The mesoporous structure (2–50 nm) of the material with narrow pore-size distribution and small pore sizes, which promote reactant access and efficient Cr(VI) adsorption, is confirmed by these values.

Following Cr(VI) treatment, cumulative pore surface area (BJH adsorption: 60.9 m^2/g; BJH desorption: 51.6 m^2/g) and cumulative pore volume (approximately 0.075–0.079 cm^3/g) both slightly increase to 72 m^2/g (an increase of roughly 2.86%). Concurrently, there is a modest rise in the average pore width (from roughly 4.8–5.6 nm to 5.1–5.9 nm). Two primary causes of this little increase are as follows: (i) the washing and cleaning procedure eliminated any remaining organic

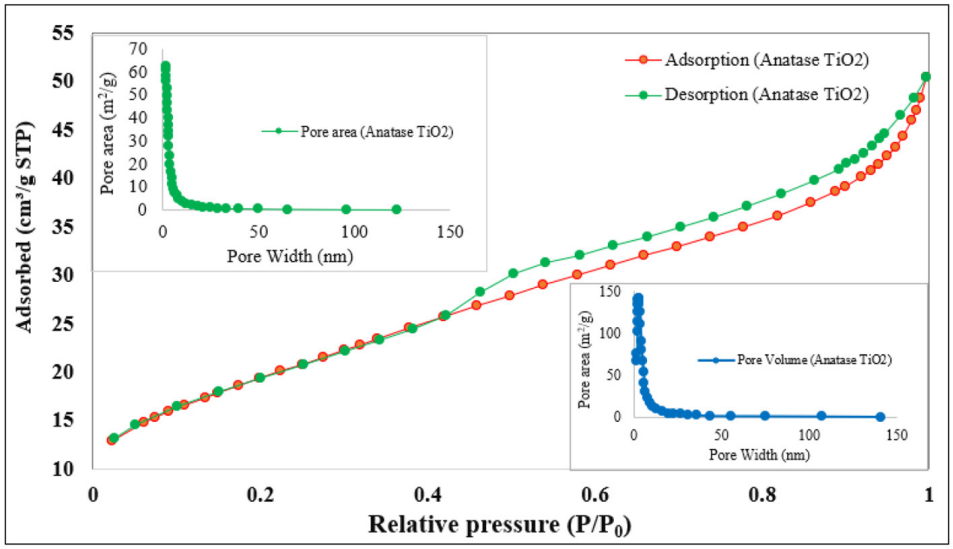

a)

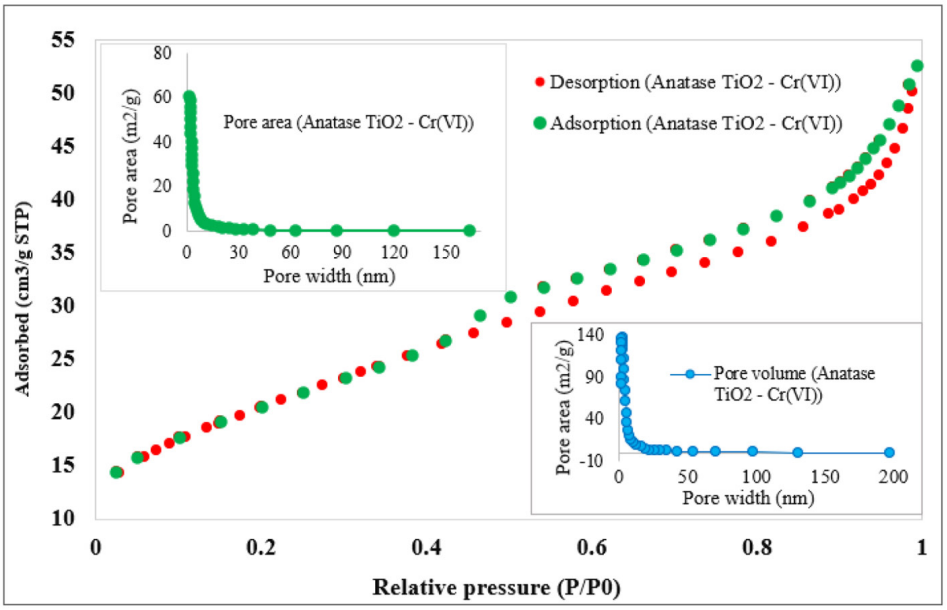

b)

Figure 11. BET results: (a) anatase TiO_2 (b) anatase TiO_2 – Cr(VI)

Table 7. BET parameters for anatase TiO_2 and anatase TiO_2 – Cr(VI)

Index	Anatase TiO_2	Anatase TiO_2 - Cr(VI)
BET Surface area	70 m^2/g	72 m^2/g
BJH Adsorption cumulative surface area of pores	62.713 m^2/g	60.9 m^2/g
BJH Desorption cumulative surface area of pores	54.4879 m^2/g	51.6 m^2/g
BJH Adsorption cumulative volume of pores	0.075867 m^2/g	0.079741 cm^3/g
BJH Desorption cumulative volume of pores	0.074848 cm^3/g	0.075278 cm^3/g
BJH Adsorption average pore width (4V/A):	4.8390 nm	5.2294 nm
BJH Desorption average pore width (4V/A):	5.4946 nm	5.8349 nm
D-H Adsorption average pore width (4V/A):	4.7949 nm	5.1625 nm
D-H Desorption average pore width (4V/A):	5.5970 nm	5.9413 nm

contaminants or tiny aggregated particles, revealing more active surface area; (ii) A minor structural alteration of the pores may result from the production and deposition of Cr(III) in the form of thin hydroxide or oxide layers on the surface. This would cause the average pore size to slightly increase without causing any major blockage. Although this behavior deviates from many conventional studies (which frequently report a decrease in surface area due to pore blocking), it stays within an acceptable range of variation and shows that the amount of deposited Cr(III) is not excessive, enabling the material to successfully maintain its mesoporous structure.

All things considered, the BET results show that following Cr(VI) treatment, the anatase TiO_2 material maintains its high surface area and stable porous structure with only very little alterations (slight increase in surface area and pore size). These results demonstrate the considerable potential of the material for reuse because of its exceptional resistance to pore blockage, in addition to confirming the efficacy of the photocatalytic Cr(VI) reduction process (in good accord with evidence from Raman spectroscopy, FTIR, and zeta potential investigations). Because of this, it is ideal for real-world uses in the treatment of wastewater that contains chromium.

CONCLUSIONS

Porous anatase TiO_2 nanostructures with an average surface area (70 m^2/g) and a mesoporous structure were successfully produced by the synthesis technique employing the chitosan-PVA template, enhancing accessibility for Cr(VI) removal. Important features such as FTIR (enhanced OH and Cr–O vibrations), zeta potential shift (−57.2 to −48.1 mV), and Raman spectroscopy (strong post-treatment fluorescence from Cr^{3+}) unambiguously confirmed the photocatalytic reduction mechanism: Cr(VI) is reduced to Cr(III), which adsorbs onto the TiO_2 surface without significantly affecting the structural integrity or stability of the suspension. These findings demonstrate the efficiency of the material in transforming extremely hazardous Cr(VI) into innocuous Cr(III), providing a low-cost, sustainable solution to industrial wastewater problems. Future research could examine doping techniques to increase the visible-light reactivity and scale up useful applications, developing environmentally acceptable pollution-control devices based on nanomaterials.

Acknowledments

The Applied Chemical-Biological Technology research group (code: 03-2025-NCTN) gratefully acknowledges the support provided by Hanoi University of Industry for the implementation of this research.

We also acknowledge HaUI Institute of Technology and Institute of Environmental Technology for laboratory support and access to analytical instruments. Financial support from Hanoi University of Industry is gratefully acknowledged.

REFERENCES

1. Hyo, W.K., Heechang, W., Eui, H.K., Ki, H.L. (2018). Water-resistant lignin/poly (vinyl alcohol) blend fibers for removal of hexavalent chromium. *Fibers and Polymers, 19*, 1175–1183. https://link.springer.com/article/10.1007/s12221-018-8052-z
2. Ghosh, A., Dastidar, M. G., Sreekrishnan, T. R.

(2017). Bioremediation of chromium complex dyes and treatment of sludge generated during the process. *International Biodeterioration & Biodegradation*, *119*, 448–460. https://doi.org/10.1016/j.ibiod.2016.08.013

3. Liang, X., Ning, X., Chen, G., Lin, M., Liu, J., Wang, Y. (2013) Concentrations and speciation of heavy metals in sludge from nine textile dyeing plants. *Ecotoxicology and Environmental Safety*, *98*, 128–134. https://doi.org/10.1016/j.ecoenv.2013.09.012
4. Farooqi, Z. H., Akram, M. W., Begum, R., Wu, W., Irfan, A. (2021). Inorganic nanoparticles for reduction of hexavalent chromium: physicochemical aspects. *Journal of Hazardous Materials*, *402*, 123535. https://doi.org/10.1016/j.jhazmat.2020.123535
5. Hu, X., Wen, J., Zhang, H., Wang, Q., Yan, C., Xing, L. (2020). Can epicatechin gallate increase Cr(VI) adsorption and reduction on ZIF-8? *Chemical Engineering Journal*, *391*, 123501. https://doi.org/10.1016/j.cej.2019.123501
6. Chaudhary, M., Maiti, A. (2020). Fe–Al–Mn@chitosan-based metal oxides blended cellulose acetate mixed matrix membrane for fluoride decontamination from water: removal mechanisms and antibacterial behavior. *Journal of Membrane Science*, *611*, 118372. https://doi.org/10.1016/j.memsci.2020.118372
7. Wang, J., Zhuang, S. (2018). Removal of various pollutants from water and wastewater by modified chitosan adsorbents. *Critical Reviews in Environmental Science and Technology*, *47*, 2331–2386. https://doi.org/10.1080/10643389.2017.1421845
8. Lei, C., Wang, C., Chen, W., He, M., Huang, B. (2020). Polyaniline@magnetic chitosan nanomaterials for highly efficient simultaneous adsorption and in situ chemical reduction of hexavalent chromium: removal efficacy and mechanisms. *Science of the Total Environment*, *733*, 139316. https://doi.org/10.1016/j.scitotenv.2020.139316
9. Çay, A., Miraftab, M., Kumbasar, E. P. A. (2014). Characterization and swelling performance of physically stabilized electrospun poly (vinyl alcohol)/chitosan nanofibres. *European Polymer Journal*, *61*, 253–262. https://doi.org/10.1016/j.eurpolymj.2014.10.017
10. Kumar, M., Tripathi, B. P., Shahi, V. K. (2009). Crosslinked chitosan/polyvinyl alcohol blend beads for removal and recovery of Cd(II) from wastewater. *Journal of Hazardous Materials*, *172*(2), 1041–1048. https://doi.org/10.1016/j.jhazmat.2009.07.108
11. Sahu, J.N., Acharya, J., Meikap, B.C. (2009). Response surface modeling and optimization of chromium(VI) removal from aqueous solution using Tamarind wood activated carbon in batch process. *Journal of Hazzardous Materials*, *172*(2–3), 818–825. https://doi.org/10.1016/j.jhazmat.2009.07.075
12. Xiaoshu, L., Jiang, G., Xue, X., Xu, X. (2013). Fe(0)–Fe_3O_4 nanocomposites embedded polyvinyl alcohol/sodium alginate beads for chromium(VI) removal. *Journal of Hazardous Materials*, *262*, 748–758. https://doi.org/10.1016/j.jhazmat.2013.09.036
13. Isawi, H. (2020). Using zeolite/polyvinyl alcohol/sodium alginate nanocomposite beads for removal of some heavy metals from wastewater. *Arabian Journal of Chemistry*, *13*(6), 5691–5716. https://doi.org/10.1016/j.arabjc.2020.04.009
14. Attia, A.A., Shouman, M.A., Khedr, S.A., Fagal, G.A. (2020). Removal of chromium(VI) from wastewater via polyvinyl alcohol and polyvinyl alcohol/chitosan encapsulated onto jojoba leaves: fixed-bed column studies. *Desalination and Water Treatment*, *190*, 203–214. https://doi.org/10.5004/dwt.2020.25663
15. Neghi, N., Kumar, M., Burkhalov, D. (2019). Synthesis and application of stable, reusable TiO_2 polymeric composites for photocatalytic removal of metronidazole: removal kinetics and density functional analysis. *Chemical Engineering Journal*, *359*, 963–975. https://doi.org/10.1016/j.cej.2018.11.090
16. Wang, H., Liang, Y., Liu, L., Hu, J., Cui, W. (2018). Highly ordered TiO_2 nanotube arrays wrapped with g-C3N4 nanoparticles for efficient charge separation and increased photoelectrocatalytic degradation of phenol. *Journal of Hazardous Materials*, *344*, 369–380. https://doi.org/10.1016/j.jhazmat.2017.10.044
17. Anaya-Esparza, L. M., Montalvo-González, E., González-Silva, N., Méndez-Robles, M. D., Romero-Toledo, R., Yahia, E. M., Pérez-Larios, A. (2019). Synthesis and characterization of TiO_2-ZnO-MgO mixed oxide and their antibacterial activity. *Materials*, *12*, 698. https://doi.org/10.3390/ma12050698
18. [19] Kochkina, N. E., Butikova, O. A. (2019). Effect of fibrous TiO_2 filler on the structural, mechanical, barrier and optical characteristics of biodegradable maize starch/PVA composite films. *International Journal of Biological Macromolecules*, *139*, 431–439. https://doi.org/10.1016/j.ijbiomac.2019.07.213
19. Huang, K. S., Grumezescu, A. M., Chang, C. Y., Yang, C. H., Wang, C. Y. (2014). Immobilization and stabilization of TiO_2 nanoparticles in alkaline solidified chitosan spheres without cross-linking agent. *International Journal of Latest Research in Science and Technology*, *3*, 174–178. https://www.mnkjournals.com/journal/ijlrst/Article?paper_id=10298
20. Xu, S., Xiao, G., Wang, Z., Wang, Y., Liu, Z., Sum H. (2021). A reusable chitosan/TiO_2@g-C3N4 nanocomposite membrane for photocatalytic removal of multiple toxic water pollutants under visible light. *Water Science and Technology*, *83*(12), 3063–3074. https://doi.org/10.2166/wst.2021.188
21. Du, X., Bai, X., Xu, L., Yang, L., Jin, P. (2020). Visible-light activation of persulfate by TiO_2/g-C_3N_4

photocatalyst toward efficient degradation of micropollutants. *Chemical Engineering Journal, 384*, 123245. https://doi.org/10.1016/j.cej.2019.123245

22. Duan, Z., Zhu, Y., Hu, Z., Zhang, J., Liu, D., Luo, X., Gao, M., Lei, L., Wang, X., Zhao, G. (2020). Micro-patterned $NiFe_2O_4$/Fe–TiO_2 composite films: fabrication, hydrophilicity and application in visible-light-driven photocatalysis. *Ceramics International*, *46*, 27080–27091. https://doi.org/10.1016/j.ceramint.2020.07.185
23. Li, Q.-H., Dong, M., Li, R., Cui, Y.-Q., Xie, G.-X., Wang, X.-X., Long, Y.-Z. (2021). Enhancement of Cr(VI) removal efficiency via adsorption/photocatalysis synergy using electrospun chitosan/g-C_3N_4/TiO_2 nanofibers. *Carbohydrate Polymers*, *253*, 117200. https://doi.org/10.1016/j.carbpol.2020.117200
24. Zainal, Z., Hui, L. K., Hussein, M. Z., Abdullah, A. H., Hamadneh, I. R. (2009). Characterization of TiO_2-chitosan/glass photocatalyst for the removal of a monoazo dye via photodegradation-adsorption process. *Journal of Hazardous Materials, 164*, 138–145. https://doi.org/10.1016/j.jhazmat.2008.07.154
25. Wiacek, A. E., Godzecka, A., Jurak, M. (2018). Physicochemical characteristics of chitosan–TiO_2 biomaterial. 1. Stability and swelling properties. *Industrial & Engineering Chemistry Research*, *57*, 1859–1870. https://doi.org/10.1021/acs.iecr.7b04257
26. Vallejo-Montesinos, J., Gámez-Cordero, J., Zarraga, R., Pérez-Pérez, M. C., González-Calderon, J. A. (2020). Influence of the surface modification of titanium dioxide nanoparticles TiO_2 under efficiency of silver nanodots deposition and its effect under the properties of starch–chitosan (SC) films. *Polymer Bulletin*, *77*, 107–133. https://doi.org/10.1007/s00289-019-02740-z
27. Jurado-Manzano, B., Rojas-Candelas, L.E., Pérez-Morales, R., Cruz-Delgado, V.J., Pérez-Pérez, M.C., González-Calderon, J.A. (2019). Improvement in the dispersion of TiO_2 particles inside chitosan–methyl cellulose films by the use of silane coupling agent. *Journal of the Mexican Chemical Society*, *63*(2), 154–168. https://doi.org/10.29356/jmcs.v63i2.741
28. Bahloul, A., Khouchaf, L., Sebbar, E., Talbi, A., Naser, E., Ech-chahed, B., Kaidi, Z., Mzerd, A. (2020). Comparison of anatase and rutile TiO_2 nanostructure for gas sensing application. *Digest Journal of Nanomaterials and Biostructures, 15*(4), 1001–1008. https://doi.org/10.15251/djnb.2020.154.1001
29. Karbassi, A., Razavi, S.M.R., Hajmohammadi, H., Yazdani, R. (2020). Synthesis, structural and electrical properties of PVA/TiO_2 nanocomposite films with different TiO_2 phases prepared by sol–gel technique. *Journal of Materials Science: Materials in Electronics, 31*, 17574–17584. https://doi.org/10.1007/s10854-020-04313-7
30. Ahmad, M.M., Mushtaq, S., Al-Qahtani, H.S., Sedky, A., Alam, M.W.A. (2021). Investigation of TiO_2 nanoparticles synthesized by sol–gel method for effectual photodegradation, oxidation and reduction reaction. *Crystals, 11*, 1456. https://doi.org/10.3390/cryst11121456
31. Huong, T.T., Trang, T.Y.D., Duc, H.T., Hien, N.T.T., Yen, P.T.T. (2025). Optimization of hexavalent chromium removal from aqueous solution by ascorbic acid treated sugarcane bagasse. *Environmental Research, Engineering and Management*, *81*(1). https://doi.org/10.5755/j01.erem.81.1.38481